UNIVERSITY OF HAWAII LIBRARY

STRUCTURE AND EXTINCTION OF SPHERICAL DIFFUSION FLAMES IN MICROGRAVITY

A THESIS SUBMITTED TO THE GRADUATE DIVISION OF THE UNIVERSITY OF HAWAI'I IN PARTIAL FULFILLMENT OF THE REQUIREMENTS FOR THE DEGREE OF

MASTER OF SCIENCE

IN

MECHANICAL ENGINEERING

AUGUST 2006

By
Karl J. Santa

Thesis Committee:

Beei-Huan Chao, Chairperson
Marcelo H. Kobayashi
Stephen M. Masutani

We certify that we have read this thesis and that, in our opinion, it is satisfactory in scope and quality as a thesis for the degree of Master of Science in Mechanical Engineering.

THESIS COMMITTEE

Chairperson

Acknowledgements

There are many people I want to acknowledge and thank for making the completion of my Master's program possible. First of all I would like to thank my advisor Dr. Beei-Huan Chao without which none of this would have been possible. I have taken more classes from Dr. Chao than from any other professor at U.H. and I believe this has played an important role in shaping my interest and work ethic. He has always pushed me to the edge of my ability while at the same time always making himself available to help with any questions I may have. Of course without the commitment of my committee members Dr. Marcelo Kobayashi and Dr. Stephen Masutani the completion of my thesis would not have been possible. I want to thank them both for taking the time to read through my thesis and provide feedback as well as not grilling me too much during my defense. Seriously though, I want to thank them both for their encouragement and cooperation during the thesis process.

O.K. before I forget I want to thank my mom and dad for their financial and emotional support throughout my college career. I still remember when I graduated from high school and didn't really want to continue in school but decided to anyway mostly because my dad gave me the ultimatum: "Either go to school or get a job and start paying rent." Who would have thought I would have stuck with it for this long. Thank you mom and dad for first believing in me so I would later believe in myself.

Last but not least I want to thank all my colleagues for helping me with questions and reminding me to have fun. In particular I want to thank Lynnette since she basically tutored me in LaTeX while I was writing my thesis. Thanks for being patient and sending me all those files *Dr. Ramirez*.

I also want to thank NASA for providing my financial support through grant NCC3-696.

Abstract

Spherical diffusion flames in microgravity were studied both numerically and experimentally. The flames are supported on a porous spherical burner which issues a constant flowrate into a quiescent atmosphere. Experiments were performed in the NASA Glenn 2.2 s and 5.2 s drop facilities. The experiments involved flames burning ethylene and propane at 0.98 bar. The numerical simulations incorporate a one-dimensional flame code with detailed chemistry and transport and an optically thick radiation model. The microgravity environment eliminates the effect of buoyancy resulting in spherically symmetric flames and increased residence times. The increased residence times inflate the Lewis number effect and radiative heat loss in the flames. Comparisons between the model and experiments reveal the model consistently over predicts the flame sizes. One explanation for the over prediction of the flame size in the model could be attributed to the fact that the thermal and mass diffusion in the code is too low. Good agreement between the experiments and model, with respect to flame size, is achieved by increasing the diffusion properties in the code by 30%. The experimental and numerical results show that when pure oxygen is issued from the burner the flame temperature is lower than the cases where fuel is issued from the burner. The lower flame temperature for the case when diluted fuel is in the ambient is expected to be a consequence of a higher than unity Lewis number. In the experiments it is hard to prove this hypothesis since the radiation for each flame is different. However, in the numerical model the radiation was turned off and the steady state flame temperatures indicate a 200 K reduction in flame temperature from adiabatic for the case with diluted fuel in the ambient. Aside from the Lewis number effect radiative extinction was also investigated. The results indicate that at high flowrates (above 5.1 mg/s) radiative extinction occurs. At high flowrates it was found that extinction time and flame temperature became independent of flowrate.

Table of Contents

List of Tables

List of Figures

Nomenclature

0	subscript refers to condition at the center of the burner
F, O	subscript denoting fuel or oxygen respectively
K	number of species
Le	Lewis number
Nu	Nusselt number
Pe	Peclet number
Ra	rate of radiative heat loss
T	temperature
T_f	temperature of the flame
V_k	diffusion velocity of species k
W_k	molecular weight of species k
Y_k	mass fraction of species k
Z_{st}	stoichiometric mixture fraction
∞	subscript refers to specified condition in the ambient
λ	conductivity
ν	stoichiometric coefficient
ω_k	reaction rate of species k
ρ	gas density
c_p	average specific heat
$c_{p,k}$	species specific heat
h_k	enthalpy of species k
q_F	heat of combustion per unit mass of fuel
r	radial spatial coordinate
t	time
u	radial flow velocity

Chapter 1

INTRODUCTION

The steep increase in the cost of gasoline, natural gas, and heating oil over the past few years has been painful and hard to ignore. In August 2004 economists were concerned when the price of oil reached $48 per barrel (Ignatius 2004). At present the price of oil hovers as high as $75 per barrel. On the positive side, the higher prices raise the awareness for conservation, motivate investment and research in alternative energy, and force innovation. On the other hand, the rising cost of fuel could trigger a recession. Several explanations have been proposed for the rising energy cost:

1. China and India's rapidly growing economies. In 1990 China and India combined consumed 5% of global oil usage while in 2003 it jumped to 12% (Carlson 2005).

2. World oil production either has peaked (Antal 2004) or will peak within the next few years (Zapka 2006).

3. Uncertainty due to instability in the middle east.

4. Damage of production facilities caused by more frequent and large scale natural disasters.

Whether it is one or a combination of factors affecting the rising energy costs the problem does not appear to be resolvable in the near future. Technologies must be developed now so that they can be implemented in time to prevent a continual decline in our standard of living. Examples of potential solutions to the problem of high fuel costs include:

1. Replacement or supplement of gasoline and diesel with additives such as ethanol and biodiesel.

2. Development of hydrogen fuel cells and hybrid automobiles.

3. Discovery and implementation of alternative energy sources such as wind, solar, geothermal, hydroelectric, oceanic, etc.

4. Improvement of the efficiency of combustion devices.

Because the technology of hydrogen fuel cells still is at its infancy and may be more than a decade away from becoming a viable energy source, and the application of alternate energy sources is limited, a more attainable short term solution involves a combination of increasing the efficiency of combustion devices and substituting ethanol and biodiesel in place of traditional petroleum based fuels. Design of combustion devices that can achieve improved efficiency requires a thorough understanding of combustion characteristics. Recognizing that most practical combustion devices, such as diesel engines, industrial furnaces and jet engines, employ nonpremixed combustion, or called diffusion flames, meaning the fuel and the oxidizer are supplied from different sources and meet in the molecular level near the reaction region, this thesis focuses on the burning behavior of a diffusion flame.

Flame extinction is an important issue in combustion systems and has been a major subject in combustion research. Undesired flame extinction in combustion devices renders a waste of precious fuel, loss of energy and production of pollutants, which in turn can lead to many consequences such as shortage of electricity supply, power loss in an aircraft and interruption of manufacturing processes in industry. On the other hand, house and wild fires need to be extinguished as fast as possible to minimize the loss of property. A flame can be extinguished for various reasons including conductive and radiative heat loss, reduction of residence time, incomplete reaction, off-stoichiometric between the fuel and the oxidizer, imbalance between the heat and mass transfer and dilution of the reactants.

Extinction of diffusion flames has been extensively investigated analytically, numerically and experimentally in laboratories using the counterflow and droplet flames because of their simplicity in geometry (Liñán 1974, Law 1975, Wu et al. 1982). Tremendous advancements in the understanding of the extinction behavior were accomplished. These

studies are steady-state or quasi-steady, and adiabatic in nature. The extinction condition is characterized by a Damköhler number, *Da*, defined as the ratio of the characteristic flow time to the reaction time. By continuously decreasing *Da*, the flame becomes weaker and is eventually extinguished. The smallest *Da* for which extinction is observed represents the kinetic limit of the flame and is identified as the kinetic extinction state. Extinction was not observed by increasing *Da* because of the enhanced burning intensity.

Recent theoretical studies, pioneered by an analytical investigation by Chao et al. (1990) using droplet combustion, further reveal that in the presence of radiative heat loss, there exists another extinction limit at high *Da* (Mills & Matalon 1998, Liu et al. 2000). That is, contrary to the conventional understanding, there exists a maximum *Da* above which a flame also extinguishes due to excess radiative heat loss. This extinction limit is termed radiative extinction limit. Radiative extinction limit has never been observed experimentally on earth because of the intrusion by the buoyancy force. The buoyancy increases with flame size, promotes mixing and reduces residence time, which in turn diminishes the radiative loss and suppresses flame extinction. For a counterflow flame, the flame becomes unstable and flashback occurs before the radiative extinction limit is reached. Moreover, because the flame is strained, the extinction limits are not fundamental limits even if the radiative extinction limit were obtainable. For droplet combustion, the droplet size needs to be increased during the burning to increase *Da*, which is unrealistic. Attempts have been made to verify the existence of radiative extinction for droplet combustion in microgravity in some space shuttle missions (Dietrich et al. 1996, Nayagam et al. 1998). Although success was reported, the conclusion is not conclusive because, as just mentioned, the droplet size can only be decreased during the quasi-steady burning. Moreover, while droplet flames can be truly spherically symmetric in microgravity, the inherent small size and unsteadiness impose limitations to the study of flame structure (Tse et al. 2001).

To obtain steady-state combustion, and avoid the effect of flame strain, this research considered spherical diffusion flames supported by a spherical porous burner. Steady-state burning can be achieved by supply of a reactant at a constant mass flow rate into a chamber

filled with the other reactant, provided that the chamber is sufficiently large comparing to the size of the burner. In addition to the simplicity in the geometry and the ability to establish a steady-state, unstrained flame, the ability to isolate the control of flow direction (convection) and inert distribution (flame structure) also make this system attractive. The bulk flow can be arranged from the fuel to the oxidizer when the fuel is issued from the burner into an oxidizing environment (normal flame) or from the oxidizer to the fuel (inverse flame) by switching the effluent and ambient reactants. The flame structure can be varied by controlling the amount of inert gas (e.g., nitrogen) that is supplied either with the fuel or the oxidizer. The change of flame structure as a result of inert distribution is frequently characterized by stoichiometric mixture fraction Z_{st}, defined for ethylene-oxygen systems as:

$$Z_{st} = \left[1 + (24/7)\frac{Y_{C2H4,0}}{Y_{O2,0}}\right]^{-1} = \left[1 + 3X_{C2H4,0}\left(\frac{1}{7} + \frac{1}{X_{O2,0}}\right)\right]^{-1} \tag{1.1}$$

where Y denotes mass fraction, X is the mole fraction, and the subscript 0 refers to conditions in the supply gas. These unique properties allow independent study of the effects of convection and flame structure. The same system has been used to study the soot inception processes and the possibility to establish high temperature, soot free flames (Liu et al. 2001, Sunderland et al. 2003, 2004).

Responding to the variation of flow direction and inert distribution, four limiting flames burning ethylene with oxygen, were adopted in this investigation. These flames are:

- Flame (a) C_2H_4 issuing into 21% O_2
- Flame (b) 8.14% C_2H_4 issuing into O_2
- Flame (c) 21% O_2 issuing into C_2H_4
- Flame (d) O_2 issuing into 8.14% C_2H_4

Nitrogen is used as the inert for all these flames. These limiting flames cover both the high and low stoichiometric mixture fraction flames, as well as normal and inverse flames.

The Z_{st} is 0.064 for Flames (a) and (c) and 0.78 for Flames (b) and (d). The convection direction is toward the oxidizer in Flames (a) and (b) and toward the fuel in Flames (c) and (d). All four flames have the same stoichiometric relations and, hence, the same adiabatic flame temperature.

The study was primarily numerical using a flame code with detailed reaction kinetics and transport data. The numerical results were compared with experiments performed by our collaborators using the microgravity facilities, including 5.2 s and 2.2 s drop towers, at NASA Glenn Research Center to assess their accuracy. To maintain spherical symmetry for both the flow field and the flame, the experiments must be performed in microgravity. Because the burning characteristics and extinction are strongly affected by the accurate description of reaction kinetics and transport properties, detailed chemistry and transport are essential to the accurate prediction of the flame response. Adoption of the Burke-Schumann reaction-sheet limit (Burke & Schumann 1928) assumes infinitely fast reaction, which cannot be used to determine the extinction state. The analysis considering the simplified one-step or reduced multi-step reaction yields results that agree with the experiments only qualitatively.

Previous studies on diffusion flames (Law & Chung 1982, Chung & Law 1983, Mills & Matalon 1997) have shown that the Lewis number, *Le*, defined as the ratio of the thermal to mass diffusion rates, have a strong effect on the flame temperature and extinction. For a spherical droplet or burner-stabilized spherical flame, the dominant Lewis number is that associated with the reactant on the ambient side of the flame (Law & Chung 1982, Chung & Law 1983). The effect of Lewis number of the reactant on the interior of the flame is secondary in general. However, it becomes evident for burner-stabilized flames at very low flowrates (Mills & Matalon 1997). For normal flames, the ambient *Le* is very close to unity while for inverse flames it depends on the property of the fuel and may have a significant deviation from unity. The effect of *Le* reduces with stronger convection across the flame (Law & Chung 1982). The effect of *Le* on the flame temperature for the four limiting flames is part of the interests in this thesis.

Both the theoretical (Tse et al. 2001) and experimental (Sunderland et al. 2003, 2004) investigations show that spherical diffusion flames stabilized by a spherical burner may not reach steady-state in 5.2 s of microgravity. These flames generally have small scalar dissipation rates which is defined as $\chi \equiv 2D(\nabla Z)^2$, where D represents the scalar diffusivity and Z is the mixture fraction. The low scalar dissipation rates result in long times to reach steady-state. The time required to obtain steady-state spherical flames is typically in the order of tens of seconds, which is beyond the capabilities of the experiments in the drop facilities. Furthermore, small scalar dissipation rates result in large radiative losses from the gaseous products, which can significantly reduce flame temperatures compared to normal-gravity flames. To allow comparison between the numerical and experimental results such that the accuracy of the numerical results can be ensured, most of the computations performed in this research are transient. Results of temperature and species concentrations, and the heat generation and loss rates for the first 5 s after the ignition or until extinction were recorded and analyzed. These results will be reported in Chapters 3 and 4. Some steady-state computations for the observation of Lewis number effects were also performed and will be reported in Chapter 3.

Chapter 2

PROBLEM DEFINITION AND METHODOLOGY

2.1 Numerical

The problem of interest is a laminar spherical diffusion flame supported by a spherical porous burner as shown schematically in Figure 2.1. A gaseous reactant with a prescribed concentration is injected from the burner at temperature T_b into an infinite quiescent environment of the other reactant at temperature T_∞. The burner is assumed to be perfectly symmetric so that both the flow field and flame are spherically symmetric in microgravity. In the course of study, the conservation equations were solved numerically using a flame code that includes detailed kinetic and transport properties. The numerical code was modified from the PREMIX (Kee et al. 1987) code which was originally developed for the study of one-dimensional freely propagating and burner-stabilized premixed laminar flames. The code was adapted for a diffusion flame in a spherical geometry and allowing for optically thick radiative heat losses. Both the steady state and transient flame behaviors can be predicted from the computations using the code.

For this problem, the equations describing the conservation of mass, energy and gas species are:

$$\frac{\partial \rho}{\partial t} + \frac{1}{r^2}\frac{\partial (r^2 \rho u)}{\partial r} = 0 \tag{2.1}$$

$$\rho c_p \frac{\partial T}{\partial t} = \frac{1}{r^2}\frac{\partial}{\partial r}\left(r^2 \lambda \frac{\partial T}{\partial r}\right) - \rho u c_p \frac{\partial T}{\partial r} - \sum_{k=1}^{K}\left(\rho c_{p,k} Y_k V_k \frac{\partial T}{\partial r} + h_k \omega_k Y_k\right) - Ra \tag{2.2}$$

$$\rho\frac{\partial Y_k}{\partial t} = -\frac{1}{r^2}\frac{\partial}{\partial r}\left(r^2\rho Y_k V_k\right) - \rho u\frac{\partial Y_k}{\partial r} + W_k\omega_k Y_k,\ k = 1, 2, \ldots, K \tag{2.3}$$

where T is the temperature, Y_k is the mass fraction of species k, W_k is the molecular weight of species k, t is the time, r is the radial spatial coordinate, u is the radial flow velocity, ρ is the gas density, c_p is the averaged specific heat at constant pressure, λ is the heat conductivity, h_k is the specific enthalpy of species k, $c_{p,k}$ is the specific heat of species k, V_k is the diffusion velocity of species k, ω_k is the production rate of species k, K is the number of species, and Ra is the rate of radiative heat loss. The equations were solved subject to the following boundary conditions:

$$r = r_b: \quad T = T_b; \quad Y_k(u + V_k) = uY_{k,b},\ k = 1, 2, \ldots, K \tag{2.4}$$

$$r \to \infty: \quad T \to T_\infty; \quad Y_k \to Y_{k,\infty},\ k = 1, 2, \ldots, K \tag{2.5}$$

where the subscripts b and ∞ refer to conditions at the burner surface and the ambient, respectively, and $Y_{k,b}$ is the value of Y_k right before the flow leaves the burner, which also is its supplied value. Because the experiments in the 5.2s drop tower showed no significant increase in the burner surface temperature during the drop, T_b was taken to be constant. The constant burner temperature can be thought of as supplying cooling water to the burner to maintain a constant temperature. For longer test times where the flame doesn't extinguish, an adiabatic energy balance should be applied at the burner surface. This boundary condition is applied in the steady state cases. Addressing the outer boundary conditions, the results indicate that after 5s the thermal field only reached a radius of 9 cm and the computations predicted no significant change in reactant compositions at the chamber wall. Therefore, while the computations assumed a finite domain ($r_{wall} = 100$ cm), it was effectively infinite and the results were not affected by this assumption (Santa et al. n.d.).

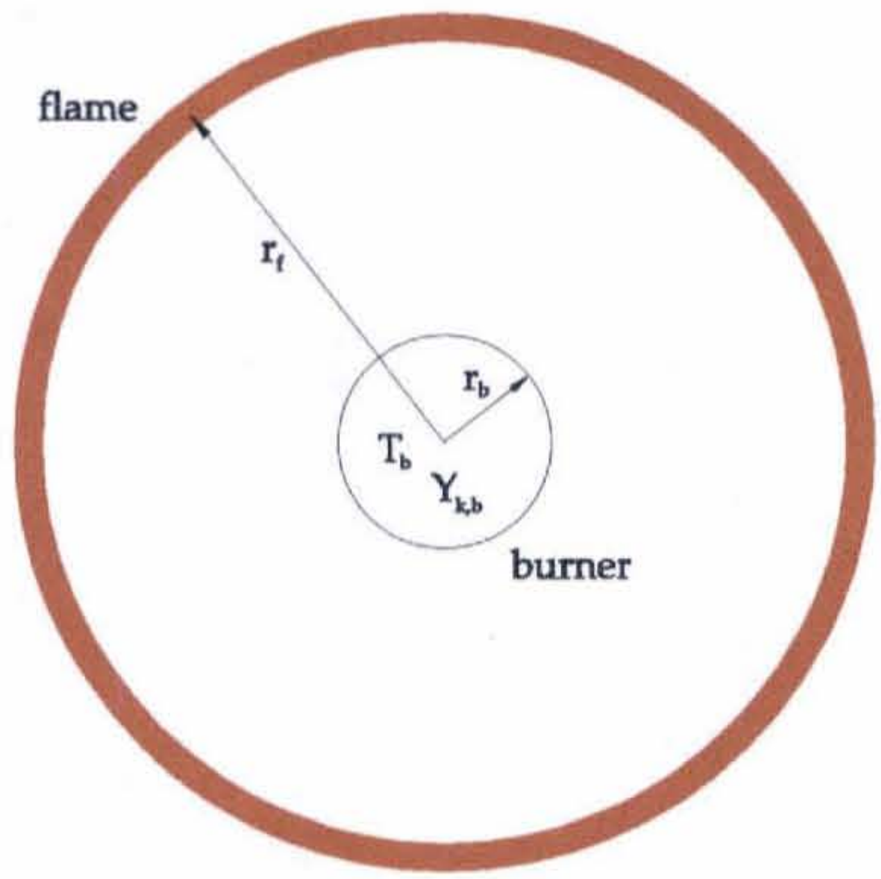

Figure 2.1: Schematic diagram for the numerical model. In the diagram, r_b is the radius of the burner, r_f is the radius of the flame, T_b represents the burner temperature, and $Y_{k,b}$ is the mass fraction of reactant k supplied from the burner.

The governing equations were discretized using conventional finite difference techniques with non-uniform mesh spacing. The transient terms were expressed by a forward difference formula, the diffusive terms by a central difference formula, and the convective terms by an upwind difference formula for better convergence (Santa et al. n.d.). The discretized equations were solved by Sandia's Twopnt code (Grcar 1992), which uses a damped Newton's method to solve transient and steady-state boundary value problems. The chemical reaction rates, thermodynamic and transport properties were evaluated by CHEMKIN and transport packages (Kee et al. 1989, 1988). The kinetics data adopted are the GRI-Mech 3.0 which contains 53 species and 325 reactions (Smith et al. n.d.).

The steady-state computations begins with a set of prescribed initial distributions of the grid points, the temperature and the species concentrations, and the location and thickness of the reaction region. If the Newton algorithm fails to converge using this initial guess, a transient integration is initiated until a user specified number of time steps has completed. The transient result is then applied as the new initial condition for another round of steady-

state integration. The procedure is repeated until a converged solution is found or the time integration extends beyond the user specified limit. Once the steady-state solution is obtained, the grid is adapted to reduce the gradients and curvature or improve the accuracy. New grid points are added until all values of the gradients and curvature are below the user specified limits, and the further addition of grid points does not affect the solution.

The primary objective of the present investigation was to understand the transient behavior of a spherical diffusion flame from its ignition. The computation requires a set of initial conditions that resemble the ignition process. Following the approach adopted by (Tse et al. 2001), the initial (ignition) conditions were prescribed as the steady-state solution of the same flame but without radiation, assuming adiabatic condition at the burner exit, and in a compressed domain to approximate the concentrated, high energy density ignition source as used in the experiments. The compressed domain normally extends between 1–5 cm from the burner exit. Application of such steady-state result as the initial condition of the transient computations was performed by expanding the domain back to the above mentioned 100 cm from the center of the burner and manually generating additional grids to fill in the gap between the compressed and normal domains. The initial values of all the variables at these extra grids are assumed to be the values at $r \rightarrow \infty$ as specified in equation 2.5.

Once the initial conditions are in place, an appropriate time interval is selected to start the transient calculations. If the computation fails to converge, the time step is reduced until a converged solution is obtained or the reduced time step is below a minimum user specified value. The grid refinement was manually performed. Upon completion of a specified number of time steps, solutions of the temperature and species concentrations, chemical heat release rate, and radiative heat loss rate at all the grid points were recorded. The flame temperature and flame location can then be extracted from the recorded temperature profile. The computation continues until the desired duration of time has been reached.

Radiation loss was included in the transient computations. The radiative heat transfer was considered to be optically thick and caused only by the participation of CO_2, H_2O, and

CO. The radiative properties of these gases were formulated by a statistical narrow-band model with a spectral bandwidth of 25 cm^{-1}. The emissivities were extracted from the line-by-line values given by the HITRAN database (Rothman et al. 2003). The discrete ordinates method, which adopted a discrete representation that included 20 different directions, was employed to account for the angular variation of the radiation intensity. The rate of radiative heat transfer was obtained by integrating over all directions using Gaussian quadrature. A more detailed description of the discrete ordinates method can be found in (Carlson & Lathrop 1968).

2.2 Experimental

Experiments were performed under microgravity conditions in the NASA Glenn 5.2 s and 2.2 s drop facilities. Microgravity, which is the condition of apparent weightlessness can only be achieved on or near Earth by putting an object in a state of free fall. One of the ways NASA conducts microgravity experiments on Earth is by using drop facilities. The drop facilities are often used to gain insight into experiments that will later be performed in the Shuttle or International Space Station. The drop testing can be used to verify or further optimize the design of the space experiments. Due to the short duration of the test time in the drop facilities, many fields of scientific research are not applicable. Combustion phenomenon on the other hand can occur very quickly which explains why combustion accounts for approximately 90% of the experiments conducted in the drop tower.

Experiments were performed in the drop facilities using a general purpose combustion rig. The rig is composed of a windowed pressure vessel supported by a fuel delivery system, an ignitor, a color CCD camera or digital still camera, a microprocessor controller, and lead acid batteries. The burner is a 6.4 mm diameter porous sphere consisting of *sintered* 10 micron stainless steel particles. The sphere is supported by a 1.6 mm stainless steel feed tube attached with epoxy. The sphere is positioned in the center of the cylindrical chamber which has a diameter, length, and volume of 25 cm, 53 cm, and 26 liters respectively (Sunderland

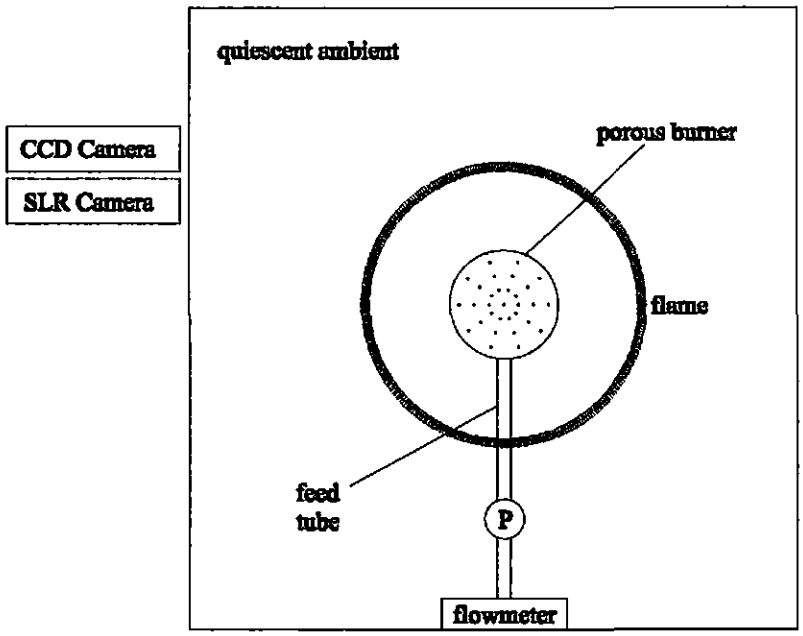

Figure 2.2: Schematic diagram of the experimental apparatus. The diagram shows the calibrated mass flowmeter and pressure regulator which delivers the feed gas through the feed tube into the porous spherical burner. The feed gas is then ejected from the burner and ignited with a quiescent ambient reactant which results in a spherical diffusion flame. The behavior of the flame during the drop is recorded by one of two cameras through a window in the pressure vessel.

et al. 2003). A schematic of the basic components of the experimental apparatus is shown in Figure 2.2.

Gas mixtures were prepared by partial pressure mixing and had an estimated composition uncertainty of $\pm$ 0.001 mole fraction. The burner feed gas was stored at 8 bar in a 75 mL bottle aboard the rig and was delivered via a pressure regulator, a solenoid valve, a fine-needle valve, a calibrated mass flow meter, and a second solenoid valve. Burner gas flowrates were measured under steady state, cold flow conditions in normal gravity about 30 minutes (for 2.2 s tests) or 90 minutes (for 5.2 s tests) before drop initiation. The flowrates were established using the mass flowmeter calibration in conjunction with gas-correction factors K_i (0.6 for C_2H_4 and 1 for O_2 and N_2) and the following relationship (Sunderland et al. 2004):

$$\frac{Indicated}{Actual flowrate} = \frac{1}{K_{mix}} = \sum_{i=1}^{2} \frac{X_i}{K_i} \tag{2.6}$$

The flow rates were verified with a soap bubble meter. Uncertainties in the flowrates are estimated at ± 10 % . Pressure decrements across the burner during flow and a nonzero plumbing volume between the second solenoid valve and the burner impose transient burner flowrates after flow commences. To minimize these transients, a pressure transducer was installed just upstream of the burner and its output was recorded at 170 Hz during each test. Care was taken to maintain a nearly constant pressure at this location to minimize the change in flowrate. Maintaining constant pressure involved opening and closing the first solenoid valve for a predetermined interval (0.25– 4 s depending on test condition) about 20 s prior to drop initiation to pressurize the plumbing system between the valves. Both solenoid valves were opened 1-2 s before drop initiation to commence flow. Before each test two purges of the chamber were performed by evacuating the chamber to 0.03 bar and filling to 0.98 bar with the appropriate ambient gas (Sunderland et al. 2003).

Microgravity laminar flames are sensitive to hydrodynamic disturbances, such as ignition before entry into microgravity, retracting ignitors, and ignition deflagrations. To minimize these disturbances, the flames were ignited within 30 ms after release into microgravity using a spring-loaded Nichrome wire with a length of 12 mm and diameter of 0.36 mm. The ignitor was energized at 28 VDC whereby it quickly glowed and ruptured. Immediately thereafter, both ends retracted with minimal wakes. The serial pair of solenoid valves facilitated smooth ignition through optimization of the initial gas discharge (Sunderland et al. 2003).

The flames were imaged using two cameras. For tests that did not involve thin-filament pyrometry (TFP) a color charge-coupled device (CCD) video camera was used. This camera had 640 × 480 pixels, 8 bits per color plane, a framing rate of 30 Hz, and a 16 mm manual-iris lens at f/1.4 (Santa et al. n.d.). Video signals were transmitted to a stationary color S-VHS video recorder via fiber optic cable. Digitized images were subsequently obtained from the

tapes using a framegrabber. Spatial resolution was 150 μm. The camera yielded flame appearance and average radius from ignition until drop termination. Except for Flame (c), flame radii were measured using the contours of peak blue emission in the video records. For Flame (c) only yellow (not blue) emissions were visible. Thus the radii for Flame (c) were measured using the inside of the contours of brightest yellow emissions. Flame diameters were determined by averaging the longest chord through each flame and its perpendicular chord; radii were then obtained by dividing the results by two.

For tests involving thin-filament pyrometry (in the 2.2 s drop tower) the video camera was replaced with a Nikon D100 consumer-grade color digital still camera. This camera has a CCD with 3008 × 2000 pixels (6 megapixels) and 12 bits per color plane. The lens that was used has a focal length of 60 mm and was set at f/8. Exposure time was 33 ms, ISO was 200, white balance was direct sunlight, and all automatic gain and focusing were disabled. Spatial resolution was 27 μm. Images from this camera were used to determine approximate peak temperatures and flame radii (Santa et al. n.d.).

The TFP method used here was based on past work (Vilimpoc & Goss 1988, Pitts 1996, Maun et al. 2006). Three silicon carbide fibers, with diameters of 13.9 μm, were strung across the flames in the camera focal plane. Before each test they were heated to glowing in lean regions of a diffusion flame to remove any deposited soot. A solenoid triggered the shutter release, whereby the camera recorded four images at times of 0.1, 0.7, 1.3, and 1.9 s after drop initiation. The filament images were smoothed using 5 × 5 pixel binning. The brightest pixel greyscale was then recorded along each of the six fiber-flame crossings and these were averaged. These average grayscales were converted to relative fiber temperatures using the previous calibration for a similar TFP system of 0.215 K/greyscale (Maun et al. 2006). These fiber temperatures were corrected for radiative loss (Maun et al. 2006). An absolute temperature reference was obtained by a thermocouple measurement of the peak temperature for Flame (d) at 1.9 s (Sunderland et al. 2003). The TFP temperatures were repeatable but have high estimated uncertainties of ± 150 K owing

to calibration uncertainties, slight soot deposition on the fibers, and incipient saturation in the red color plane for the methane test.

Gas-phase temperatures were measured with an uncoated B-type thermocouple with a wire diameter of 51 μm and a butt-welded junction of the same diameter. To minimize disturbances, the thermocouple supports were placed 20 mm apart. The thermocouple was held in a fixed position tangential to the flame. The positions were chosen, for each test, so that the expanding flame passed the junction approximately 0.8 s before drop termination. The thermocouple response was monitored at 300 Hz and the temperatures were recorded (Sunderland et al. 2003). For some tests a K-type thermocouple bonded to the burner surface was used to measure the surface temperature.

The gas-phase temperatures were obtained by correcting for the radiative loss from the thermocouple. This was done by balancing the radiative loss from the thermocouple against the convective heating assuming steady-state conditions. The thermocouple was assumed to radiate as a graybody with an emissivity of 0.2 (Bradley & Entwistle 1961). The heat transfer coefficient was obtained from the relationship of Nakai and Okazaki (1975).

$$Nu = [0.8237 - \ln(Pe/2)]^{-1} \qquad for\ Pe < 0.2 \tag{2.7}$$

The Nusselt and Peclet numbers were based on the wire diameter and transport properties of nitrogen at the average of the thermocouple and gas temperature. The identification of Pe required specifying a local velocity. The local velocity was estimated based on steady-state conservation of mass from the burner to the flame, where a molecular weight of 28 g/mole was used. Nu was found to range from 0.21 to 0.33. The corrected temperature measurements have estimated uncertainties (at the 95% confidence level) of $\pm$ 50 K (Sunderland et al. 2003).

Chapter 3

MODEL VS. EXPERIMENTAL RESULTS

This chapter addresses the work undertaken to determine the accuracy of the numerical model and explain any discrepancies that arise between the model and experiments. The effect of Lewis number on flame temperature is also addressed. The first issue of concern, regarding the accuracy of the model, was whether the flame size predicted by the model was consistent with the experiments. Several tests, using ethylene as the fuel, were performed in the NASA Glenn 5s drop tower. The results from the experiments were used to construct the history of the growth of the flames over time. The model was then used to simulate the experiments and the results for flame sizes are compared. Figure 3.1 shows measured and predicted flame radii for ethylene Flames (a) – (d). The flame radius in the model was assumed to be the point of maximum temperature. Referring to Figure 3.1, all flames are seen to grow with time, but Flames (b) and (c) approached steady-state more rapidly than Flames (a) and (d). The initial growth can be understood from the fact that diffusion flames stabilize where the fluxes of oxidizer and fuel are in stoichiometric proportions. The consumption of the ambient reactant over time diminished the gradient which reduces the flux to the flame. In response, the flames expand to reduce the burner reactant flux at the flame. The variation of flame radii with time predicted by the model qualitatively matches the experiments. The initial difference in slopes is likely due to the differences in initial (ignition) conditions and a slight unsteadiness in the burner flowrate in the experiments. The measured radius of Flame (c) agrees reasonably well with that predicted by the model despite the flame-sheet being obscured by soot in the experiments. While the trends for Flames (a), (b), and (d) predicted by the model closely resemble those of the experiments, the model consistently predicts larger flames. A similar discrepancy was observed in a previous study (Atreya & Agrawal 1998). The discrepancy was accounted for by noting that

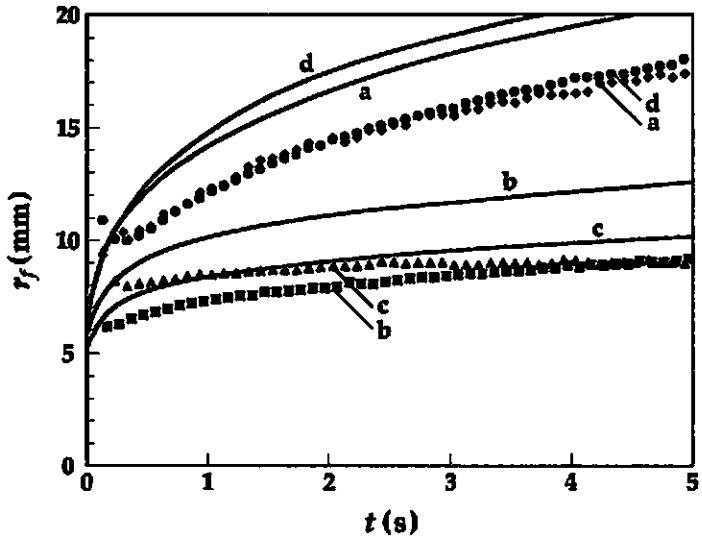

Figure 3.1: Predicted and measured flame radii for four ethylene flames: (a) C_2H_4 issuing into 21% O_2, (b) 8.14% C_2H_4 issuing into O_2, (c) 21% O_2 issuing into C_2H_4 and (d) O_2 issuing into 8.14% C_2H_4. The curves are transient numerical results while the symbols represent experiments in the 5.2 s drop facility The modeled radii correspond to peak temperatures. The measurements were derived from video records.

the peak temperature occurs on the oxidizer side of the visible flame. While this approach would improve the agreement for the normal flames it would enhance the discrepancy between the model and experiments for the inverse flames. Although the source of the disagreement remains unclear, it could arise from mass and thermal diffusion properties that are too low in the model or from experimental flow rates that are lower than reported. Transport properties are based on the Lennard-Jones potential model (Hirschfelder et al. 1964), which can underpredict transport properties of light species by up to 25% (Paul & Warnatz 1998, Middha et al. 2002).

To understand the effect of thermal and mass diffusion properties on flame structure, a parameter was added to vary the diffusion properties. Increasing the diffusivity from the Transport code (Kee et al. 1988) by 30% resulted in good agreement with the experiments. The results for Flames (a), (b), and (d) are shown in Figure 3.2. Flame (c) was excluded due to its soot obscuration. Since both the thermal and mass diffusion were changed, the

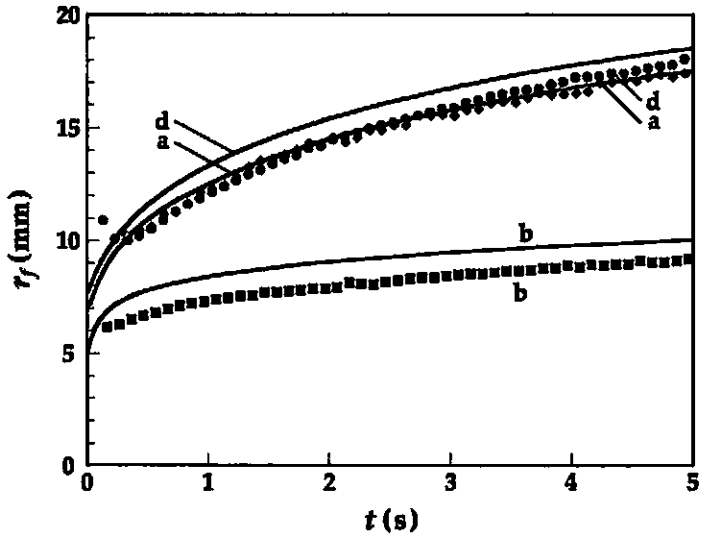

Figure 3.2: Predicted and measured flame radii similar to Figure 3.1 except the thermal and mass diffusion in the model has been increased by 30%: (a) C_2H_4 issuing into 21% O_2, (b) 8.14% C_2H_4 issuing into O_2, (c) 21% O_2 issuing into C_2H_4 and (d) O_2 issuing into 8.14% C_2H_4.

Lewis number and adiabatic flame temperature remain unchanged. A similar improvement is observed from a reduction of 25% of the model's mass flow rate, but this exceeds the estimated uncertainty of 10% for the flow rate in the experiments. Perhaps the disagreement between the model and experiments arises from errors in both the flowrate and diffusion properties. Since the source of discrepancy between experiment and theory is uncertain, the unmodified transport properties will be used in the remainder of this work.

Predictions of transient flame temperatures for the four ethylene-fueled flames are shown in Figure 3.3. After an initial increase, the flame temperatures are expected to decrease with time due to radiation. Although all four flames have the same adiabatic flame temperature, the temperatures of Flames (a) and (d) are markedly lower than those of Flames (b) and (c). Judging from Figure 3.1, Flames (a) and (d) are roughly twice the size of Flames (b) and (c). The larger flames experience greater radiative losses resulting in decreased flame temperatures. Also shown in Figure 3.3 are measured flame temperatures taken 2 s after ignition in the 2.2 s drop tower (Sunderland et al. 2003). The measurements were made with

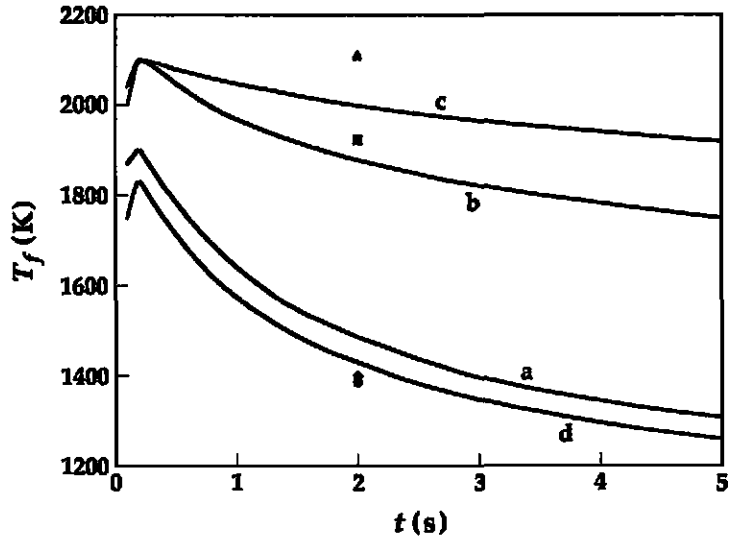

Figure 3.3: Evolution of flame temperature with time for ethylene Flames (a) through (d). The curves represent transient numerical results while the symbols represent experimental results in the 2.2s drop tower.

thermocouples and include radiation corrections. The agreement between the measured and model temperatures are within experimental uncertainties for flames (a), (b), and (d) but flame (c) has a significantly higher temperature in the experiment than in the model.

To understand the basic structural differences in the four flames, the transient and radiative heat loss effects were removed. Steady-state calculations without radiation were performed and the results are plotted in mixture-fraction space in Figure 3.4. Owing to the diffusion of nitrogen and products to the burner surface, the predictions for Flames (a) and (d) do not extend to Z_{st} of 1 and 0, respectively. The diffusion of nitrogen and products to the burner surface occurs since compositions at the surface are not specified but result from a convective-diffusive balance. Such diffusion does not occur in Flames (b) and (c) due to their higher burner flowrates. It might be expected, that since the flames all have the same equilibrium adiabatic flame temperature and there is no heat loss to the burner in the steady-state simulation, the flames would all have the same flame temperature. In spite of these conditions the flames do not have the same flame temperatures. Flames (a) and (c) have the same Z_{st} and as expected their flame temperatures are very close. Flames

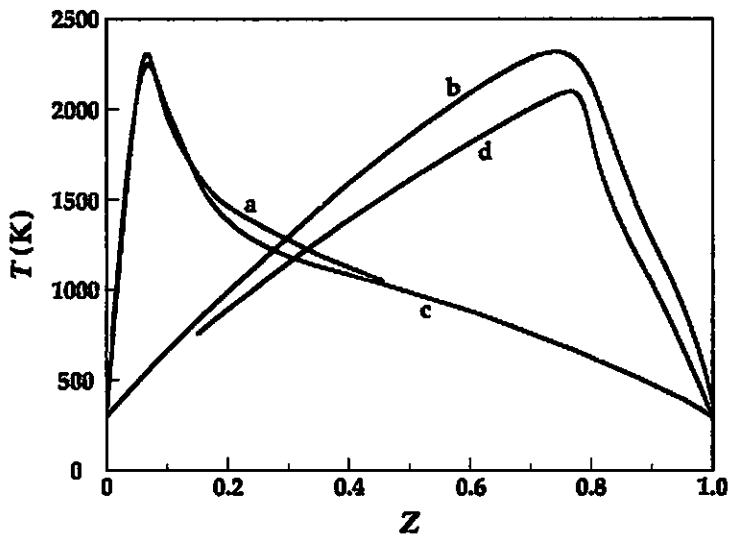

Figure 3.4: Steady-state adiabatic temperature distributions for ethylene Flames (a) through (d) as a function of mixture fraction.

(b) and (d) on the other hand, also have the same Z_{st} but Flame (d) is about 200 K cooler than the other three flames.

Two factors may be attributed to the reduced temperature of Flame (d) in the steady-state simulation. One possibility is that Flame (d), unlike Flame (b), has fuel in the ambient, which may lead to a loss of intermediate species to the ambient. The other explanation may be that the Lewis number, *Le*, of the ambient reactant may be higher in Flame (d) than in the other three flames. The Lewis number of the ambient reactant is defined as the ratio of the thermal diffusivity of the mixture to the mass diffusivity of the reactant in the ambient. Figure 3.5 shows the steady-state results for the distribution of major products and fuel for Flame (d). Significant losses of CO, H_2, and C_2H_2 are evident, although the net effect of this loss is only to shift the flame location to a region where the relative amount of nitrogen is greater. The shift is not significant enough to account for the 200 K reduction in flame temperature. While a decrease in flame temperature can occur when the *Le* differs from unity, a 200 K reduction might be considered large for a flame whose Lewis number is

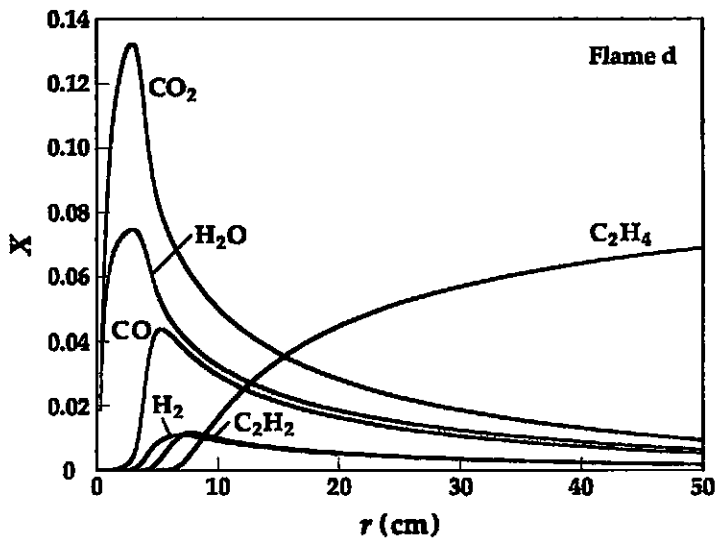

Figure 3.5: Steady-state adiabatic solutions of major products for ethylene Flame (d): O_2 issuing into 8.14% C_2H_4.

considered close to unity. It's known that for spherical droplet and spherical burner flames, the dominant *Le* affecting flame temperature is that associated with the mixture on the ambient side of the flame (Chung & Law 1983, Mills & Matalon 1997). The ambient-side *Le* for Flames (a) – (c) is near unity, whereas for Flame (d) it is expected to be slightly higher because the diffusivity of ethylene is slightly less than that of nitrogen. To observe the fundamental effect of non-unity *Le*, computations were performed for Flame (d) in steady-state, with Le_F equal to, greater than, and less than unity. The computations employed a simplified one-step reaction in the reaction sheet limit. That is, the reaction rate was set to be sufficiently fast such that further increases in reaction rate would not change the solution. The diffusivities for all species were the same. Figure 3.6 shows the results for simulations with Le_F equal to 0.9, 1.0, and 1.1. With a 10% increase/decrease in Le_F, the flame temperature drops/increases by about 200 K, which qualitatively agrees with findings of (Law & Chung 1982). The results strongly suggest that the expected difference in *Le* between Flame (d) and the other three flames accounts for the 200 K difference in flame temperature.

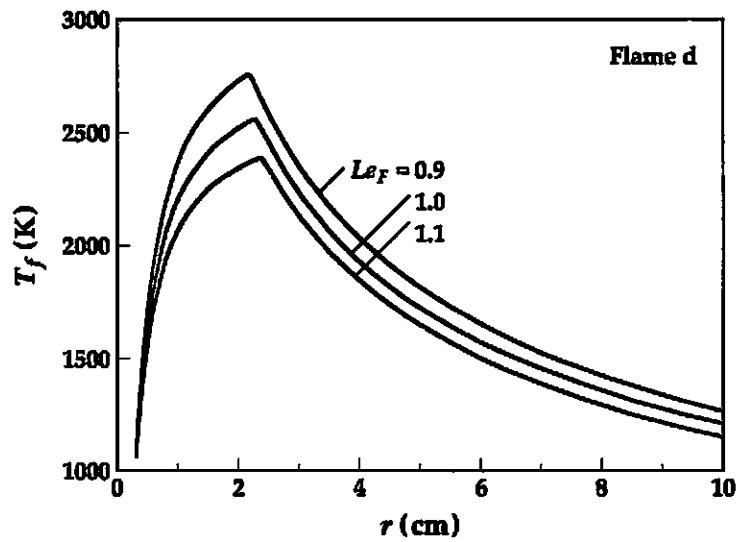

Figure 3.6: Steady-state adiabatic solution of temperature profiles for ethylene Flame (d) with Lewis number of 0.9, 1.0, and 1.1. A one-step, reaction sheet limit was used in the simulation.

To better understand the effect of Lewis number, an analytical analysis that employs the Burke-Schumann reaction sheet limit with constant transport properties but allows for different Lewis numbers on the fuel and oxidizer side of the flame was performed for the inverse flame. The solution yields the flame temperature given by:

$$T_f = \left(T_0 + \frac{\nu_F W_F q_F}{\nu_O W_O c_p} Y_{O,0}\right) - \left(T_0 + \frac{\nu_F W_F q_F}{\nu_O W_O c_p} Y_{O,0} - T_\infty\right)\left(\frac{\nu_F W_F Y_{O,0}}{\nu_F W_F Y_{O,0} + \nu_O W_O Y_{F,\infty}}\right)^{1/Le_F} \tag{3.1}$$

where Y is the mass fraction, ν is the stoichiometric coefficient, W is the molecular weight, q_F is the heat of combustion per unit mass of fuel, c_p is the specific heat at constant pressure, the subscripts F and O denote fuel and oxidizer, and the subscripts 0 and ∞ represent specified conditions at the center of the burner and the ambient. In equation 3.1, Le_F is the Lewis number of the fuel, which in the analysis is the ambient reactant. As expected, the flame temperature depends solely on the Lewis number on the ambient side of the flame. In addition, the temperature increases when Le_F is less than unity and decreases

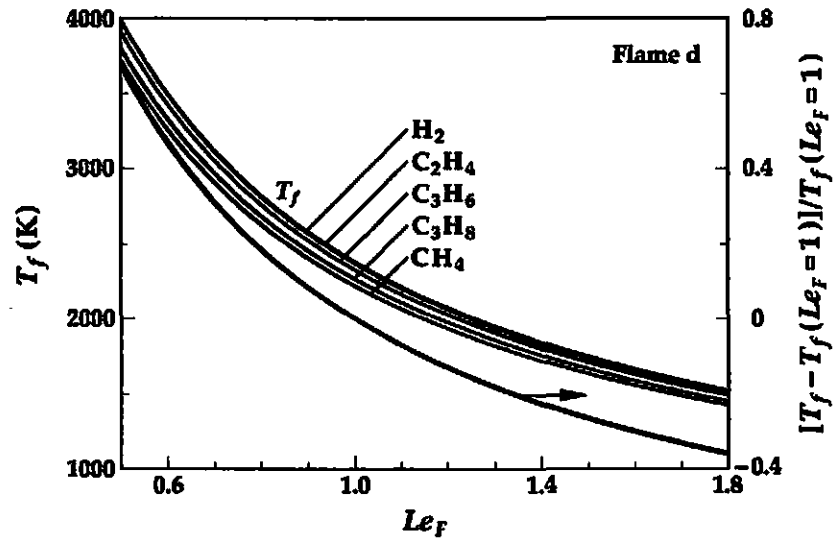

Figure 3.7: Flame temperature versus Lewis number for Flame (d) for selected fuels. The lowest curve represents, for all fuels, the fractional change of flame temperature from the unity Lewis number Flame.

when it is greater than unity. These results are consistent with the numerical results and agree with earlier studies (Chung & Law 1983, Mills & Matalon 1997). Using equation 3.1, the flame temperatures for different fuels were calculated to see if the *Le* effect was fuel dependent. The Chemical Equilibrium with Applications (CEA) code (McBride & Gordon 1996) was used to calculate the adiabatic flame temperature for each flame. The value of q_F/c_p was adjusted until equation 3.1 gave a flame temperature equal to the adiabatic case with $Le_F = 1$. The results for different fuels with varying Lewis numbers using equation 3.1 are shown in Figure 3.7. Figure 3.7 demonstrates that all flames have the same qualitative behavior in that the flame temperature reduces with increasing *Le*. In Figure 3.7 the data collapses to a single curve when the change in temperature is considered realative to the temperature at unity *Le*. This indicates that the relative change of temperature is independent of fuel type. Consistent with Figure 3.6, when Le_F is near unity, a 10% increase in Le_F results in around a 200 K decrease in flame temperature or an 8% change.

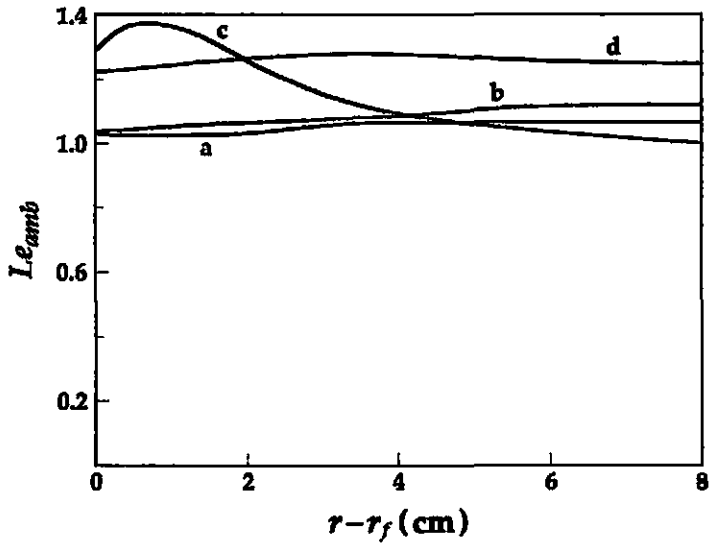

Figure 3.8: Steady-state adiabatic solution of temperature profiles for ethylene Flame (d) with Lewis number of 0.9, 1.0, and 1.1. A one-step, reaction sheet limit was used in the simulation.

This effect increases with decreasing Lewis number, as previously reported (Law & Chung 1982).

In order to verify that the ambient Lewis number for flame (d) was higher than the other three flames in the numerical code (with detailed chemistry and transport), the thermal and mass diffusion properties of all four ethylene flames were extracted from the code. The distribution of the thermal and mass diffusion properties were used to calculate the Lewis number of the ambient reactant. A plot of the Lewis number distribution for the four flames is shown in Figure 3.8. These results were obtained from the steady-state computations without radiation. This plot along with Figure 3.4, gives insight into the quantitative effect an ambient Lewis number will have on the flame temperature when detailed chemistry is considered. A distance of 8 cm from the flame sheet was chosen to be the domain of interest because diffusion of the ambient reactant is most important in this region. For this reason the ambient Le can be taken at $r - r_f = 8cm$. For Flames (c) and (d), the values of Le_F between the flame and 4 cm beyond are irrelevant because much of the fuel is pyrolyzed to other intermediate species before entering this region. Notice that Flame (d) has the

				$T_{max} - T_{max,C2H4}$,K	
Burner Gas	m_{O2}, mg/s	Ambient Gas	$X_{fuel,ambient}$	measured	modeled
O_2	5.85	CH_4/N_2	0.14	322*	152
O_2	5.18	C_2H_4/N_2	0.0814	0	0
O_2	4.49	C_3H_8/N_2	0.058	-275	-117

Table 3.1: Measured and modeled flame temperatures 1.9 s after ignition for inverse flames of three hydrocarbon fuels. *Lower bound owing to incipient saturation in the thin-film pyrometer.

largest ambient *Le* as expected. Looking at Figure 3.8, one might argue that the difference between the ambient *Le* between flames (b) and (c) is about 10% but there is no perceptible difference in flame temperatures for these two flames. Although it was stated earlier that a 10% change in *Le* could result in a 200K drop in flame temperature this applied to flame (d) which is a low convection flame. Flames (b) and (c) are high convection flames and the high convection or blowing reduces the *Le* effect (Law & Chung 1982). Instead of varying the Lewis number by changing the fuel, a variation in *Le* for a given fuel can be attained by changing the inert. For example, instead of using N_2 as the inert, if He were used, an increase in *Le* would occur, while using CO_2 would result in a decrease.

The flame temperature measurements and predictions of Figure 3.3 do not indicate a significant reduced temperature of Flame (d) as witnessed in Figure 3.4. Therefore experimental validation of the predicted flame temperature variation with ambient *Le* was sought. Three flame configurations were observed in the 2.2 s drop tower with the thin-filament pyrometer and were modeled. These are Flame (d) and corresponding flames burning methane and propane fuels, as summarized in Table 3.1. Fuel dilution levels were selected such that the adiabatic flame temperatures of the three flames was 2370 K. Also, flowrates in Table 3.1 were selected such that the ethylene and propane flame sizes were similar at 1.9 s, but limited access to the drop tower resulted in the methane flame radius being about 10% smaller. The similar flame sizes corresponded to similar radiative losses and thus any temperature difference was assumed to be attributed to the *Le* effect. Relative to Flame (d), the ambient *Le* of the methane flame is lower and that of the propane flame is higher.

The measured relative temperatures shown in Table 3.1 were determined by thin-filament pyrometry (TFP). Compared to Flame (d), these results reveal that the methane and propane flames have increased and decreased flame temperatures, as is expected from their ambient Lewis numbers. Transient numerical predictions, also shown in Table 3.1, support these trends. The agreement between measured and modeled relative temperatures is adequate given uncertainties in the TFP measurements and possible residual ignition effects.

Chapter 4

RESULTS FOR RADIATIVE EXTINCTION

The results presented in this chapter involve extinguishing flames. Both kinetic and radiative extinction were observed. The extinction was classified as kinetic (aka diffusive) when a reduction in flowrate would decrease the time to reach extinction although since the flames still experienced radiative loss the extinction could not be labeled as purely kinetic. The extinction was categorized as radiative when the time to reach extinction became independent of flowrate. The primary concern was to observe radiative extinction both numerically and experimentally and understand the factors that led to radiative extinction. Both ethylene and propane fuels were used. The ethylene flames studied were inverse flames were pure oxygen was issued from the burner into a mixture of 4% ethylene with nitrogen as the inert. The propane flames were normal flames where propane flowed from the burner into an atmosphere of 17% oxygen. The concentrations of the ambient reactant in each case were chosen so that the extinction would occur within 2s. This was necessary for the extinction to be observed experimentally in the 2.2s drop tower. For each fuel the flowrate was varied between two extremes. On one end the flowrate was reduced until ignition was no longer possible or the flame extinguished very quickly. The other extreme was realized by increasing the flowrate in the experiments until the flame became very oblong and specifying a diameter became meaningless. Once the experimental limit was reached (high flowrate) the numerical code was used to observe extinction at higher flowrates. For each fuel the effect of flowrate on extinction was examined.

Two modes of extinction onset were observed in the experiments. For low flowrates base extinction was observed, where extinction started at the base of the flame near the burner supply tube. For high flowrates hole extinction was detected, where extinction started at a single flame hole in the blue flame sheet away from the burner tube. Base or

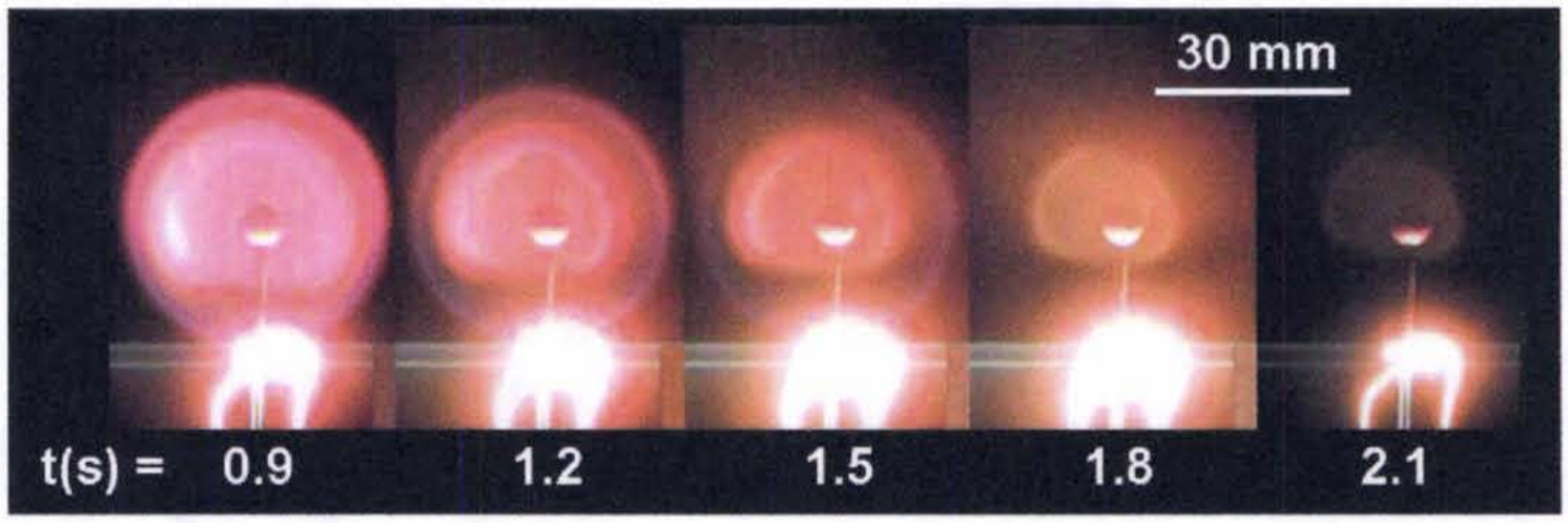

Figure 4.1: Time sequence of color images of extinguishing flame of propane flowing into 17% oxygen at 1.35 mg/s with heating wire. The thin round blue ring is the flame sheet, the kidney shaped red-orange region is soot, and the white region is the heating wire. The spherical burner and feed tube are also visible here. Hole extinction occurred at 1.47s.

hole extinction often led to complete extinction, where all flame luminosity disappeared. Extinction times reported here are referenced to the time datum at ignition. For flames in which base extinction was observed, extinction time is reported as the time when 50% of the flame surface was no longer visible. For flames in which hole extinction was observed, hole extinction time is reported as the time when a hole was first visible.

Figure 4.1 illustrates a sequence of photographs during a drop in which hole extinction occurs. Ignition occurs approximately 30 ms after the release of the rig and the onset of microgravity. The faint line surrounding the luminated region represents the flame. The kidney shaped orange luminous region around the sphere represents soot produced during the early stages that is trapped thermophoretically within the flame. The glow of the heating wire is visible at the bottom. For this flame, propane is flowing into an atmosphere of 17% oxygen. After about 1.5s, a hole is observed in the flame zone between 10 and 12 o'clock. The absence of the visibility of the flame indicates hole extinction. Soon thereafter the flame completely extinguishes and only the residual soot remains.

It might be expected that base extinction is an artificial extinction resulting from heat loss to the feed tube. To address this issue, experiments were done with the addition of a heating wire to the feed tube to observe whether it affected the extinction. Figure 4.2 illustrates extinction for propane flowing into air with and without the heating wire.

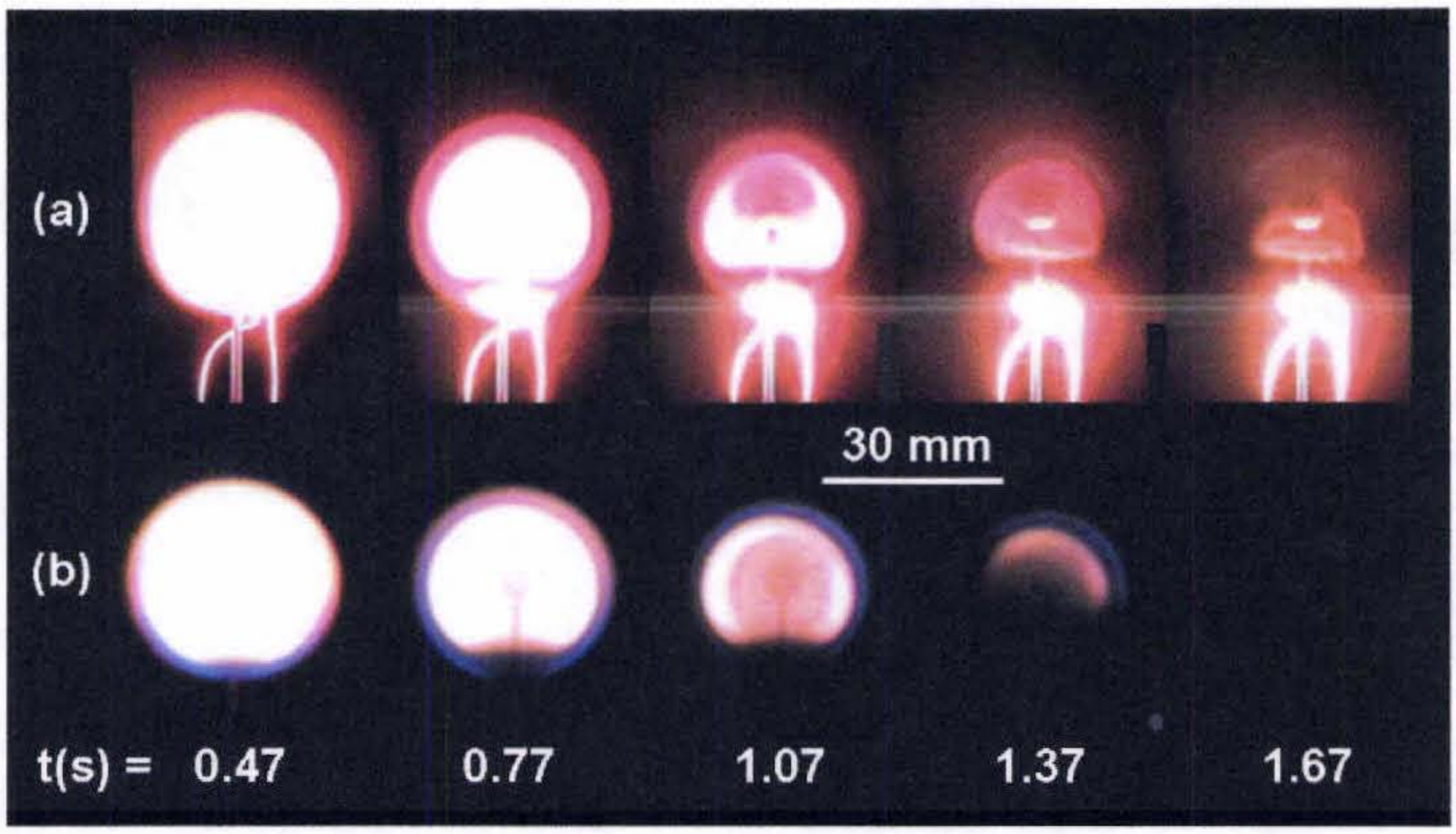

Figure 4.2: Time sequences of color images of extinguishing flames of propane flowing into air at 0.75 mg/s, (a) with heating wire, and (b) without heating wire. The visible features are similar to those described in Fig. 3.8 caption. Base extinction occurred in both cases, at 1.37s and 1.33s, respectively.

Observing the shape of the flames, it can be assumed that the flowfield is uniform. Looking at the results, extinction occurs at about 1.4 s for both cases, indicating that the time to extinction is not significantly influenced by heat loss to the burner supply tube. The edge flame and unburned region at the supply tube do not influence the bulk of the flame. Based on this, it was assumed that base extinction is an appropriate indicator of extinction within the experimental uncertainties, and thus most tests were performed without the heating wire.

Since the experiments in the drop tower are intrinsically transient, a transient numerical scheme was used to study the flames. There are two important considerations with respect to the accuracy of the numerical results: one is the grid spacing, and the other is the initial condition. The grid spacing and domain size were adjusted to ensure that the results were not dependent on them. Addressing the accuracy with regard to initial condition is a little harder since it is not possible to know what the true initial conditions are. Experimentally

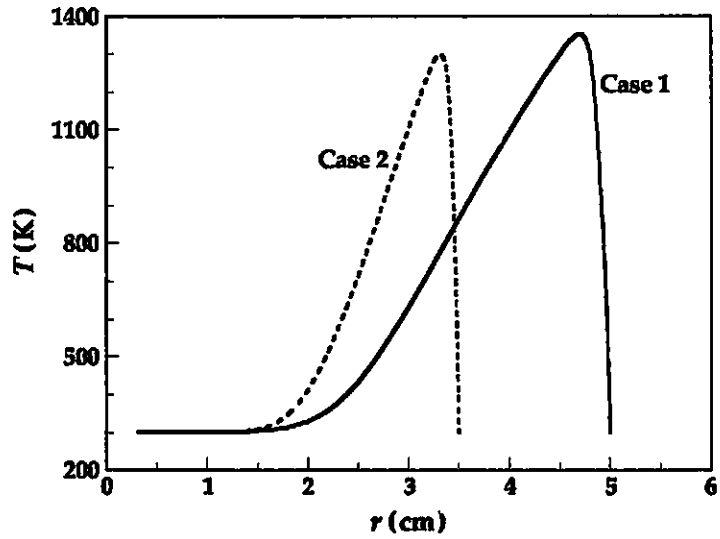

Figure 4.3: Modeled radial temperature profiles for two initial conditions for flame of oxygen flowing into 4% ethylene at 104 mg/s. The two cases are steady-state solutions without radiation and with outer boundaries at 3.5 and 5 cm.

the flow through the porous sphere begins about 2 s before ignition. Under these conditions one would expect that there is a temporary premixed flame that quickly transitions to a diffusion flame. The almost instantaneous establishment of a diffusion flame at some distance from the burner is the critical feature of this ignition. The instantaneous diffusion flame would yield steep gradients on either side of the flame. To simulate this ignition process, the approach of (Tse et al. 2001) was used to obtain our initial condition. In this approach, the initial condition is given by the compressed steady-state solution of the flame without radiation. This is done by forcing the outer boundary closer to the porous sphere. In this way, a thin flame with a composition that is similar to what would be expected for the actual flame is produced. In addition, since the flame is very thin, the radiative losses immediately after ignition are negligible. Figure 4.3 shows temperature profiles for two ignition sources with different levels of compression (domain size). Figure 4.4 illustrates the transient temperature and flame diameter resulting from the two different ignition conditions of Figure 4.3. The general characteristics of the flame history are an initial increase in flame temperature, followed by a gradual reduction in temperature until

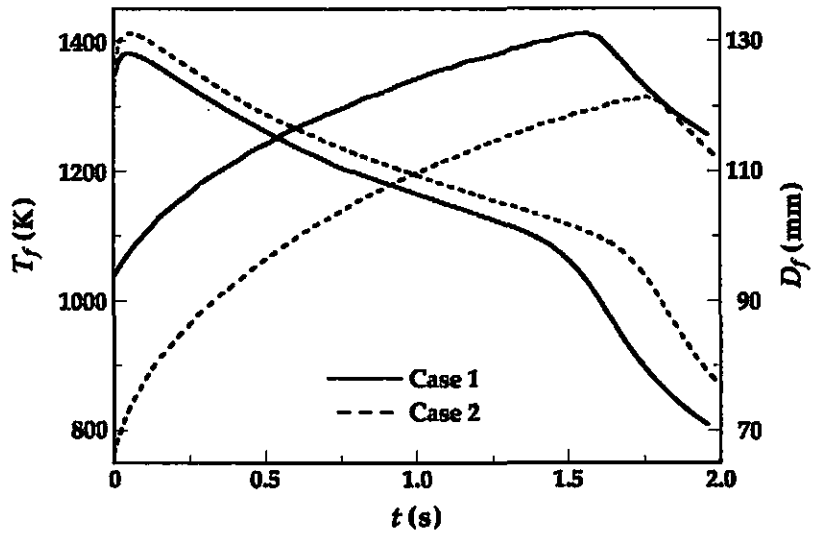

Figure 4.4: Modeled flame temperature and diameter predictions for flame of oxygen flowing into 4% ethylene at 104 mg/s for the two initial conditions of Fig. 3.10. Extinction begins when the flame diameter starts to decrease. Cases shown are for high flowrate with negligible burner heat loss.

extinction. The flame diameter continually increases until extinction is reached. The two different initial conditions of Figure 4.3 led to slightly different results, including flame size, temperature, and time to extinction. The basic trends of these results are similar to those of (Tse et al. 2001) in that radiative losses appear to dominate the flame, leading to a continuous reduction in flame temperature and eventually extinction. The initial rise in temperature occurs due to the fact that the compressed solution, although there is no radiative heat loss, experiences significant heat loss to the outer wall. Initially, when the flame is expanded to the larger domain there is no heat loss to the outer wall (shifted to 100cm) and the radiation is negligible which results in a peak in the flame temperature (peak temperature) which is higher than the flame temperature of the steady-state solution. Thus, there is an immediate rise of the temperature from ignition until radiative losses increase and the temperature begins a steady decline. Case 1 has a lower peak temperature than Case 2 since the flame is larger and suffers greater radiative loss. The considerably high

mass flowrate of these flames results in a negligible temperature gradient near the burner and therefore no conductive loss.

Numerically, the time when extinction occurs is defined as the point at which the flame diameter reaches a maximum since when the flame extinguishes the location of the flame temperature stops growing when the flame stops consuming reactants. After heat release ceases, the maximum temperature decreases due to heat dissipation. From Figure 4.4 it is evident that the diameter provides a more sensitive indicator of extinction than does temperature. Notice that hole or base extinction (as discussed in the experiments) is meaningless in the numerical model because the equations are for a 1-D flame. This is why the experiments are considered invalid at high flowrates were symmetry is no longer observed.

The criterion employed for identifying the appropriate initial condition was to compress the steady-state solution until further compression would prevent ignition, presumably because heat loss was to great. By maximizing compression, the radiation is minimized by minimizing the volume of radiating species. Following this approach, the peak temperature after ignition was found to be nearly constant for higher flowrates. The lower flowrates suffered from burner heat loss which diminished or eliminated the peak temperature. Recall that in the steady-state case the burner is heated from the flame, whereas, in the transient case with radiation, the burner temperature is fixed at 300 K and considerable heat loss is experienced by the smaller flames.

Experimental and numerical results for oxygen issuing into 4% ethylene are shown in Figure 4.5. The experimental data is given by the solid symbols. The numerical results are represented by the symbols connected by a line. Both the time to reach extinction and the diameters of the flames at extinction are plotted. From the experiments, two types of extinction are shown: base and hole extinction. Both indicate the time after ignition at which extinction is observed. At later times, the entire flame will extinguish but the times presented are more representative of the onset of extinction. The diameter of the flame at extinction is also shown. For the present range of experimental flowrates,

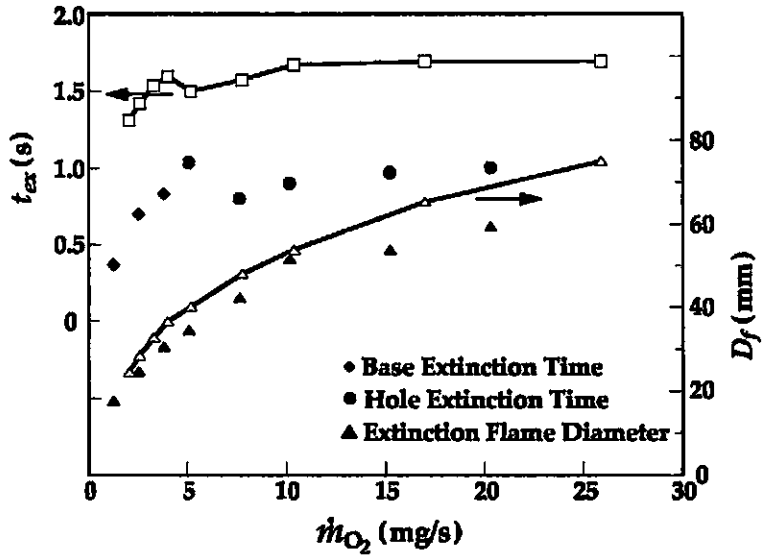

Figure 4.5: Measured and predicted extinction times and extinction diameters for flames of oxygen flowing into 4% ethylene at various flowrates. The experimental results are represented by the solid symbols and the numerical results are correspond to the symbols connected by a line. No heating wire was used in these experiments.

there is good agreement between the experiment and computation for the extinction flame diameters. Experimental results above flowrates of 22 mg/s were not beneficial due to flow non-uniformities and the onset of oblong flames. Numerical computations show that flame size increases with flowrate and the extinction diameters roughly scale with the square root of flowrate. The trends for the variation in extinction time with flowrate are similar for experiment and computation. Initially the extinction time increases with flowrate reaches a peak, experiences a short reduction and then starts to increase again and finally at a flowrate of about 10 mg/s it levels off, asymptoting to about 1 s for the experiments and 1.7 s numerically. At low flowrates, the shorter extinction time is due to the reduction in flame temperature by burner heat loss. The lower temperature, resulting from greater heat loss to the burner, requires less time to reach the extinction temperature. Although there is burner heat loss, the trigger for extinction is radiative heat loss, not burner heat loss. In other words, for the lower flowrate cases, the enthalpy that is removed from the gas mixture due to burner heat loss is significant and thus extinction occurs at shorter times.

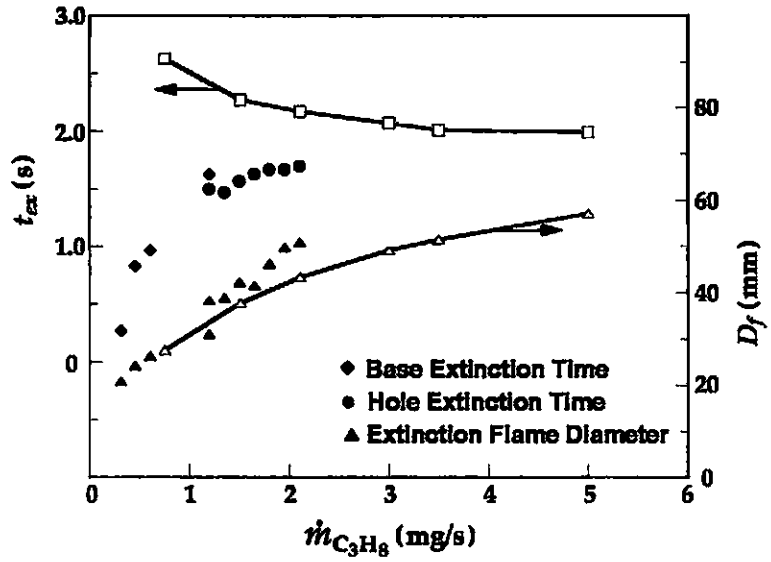

Figure 4.6: Measured and predicted extinction times and extinction diameters for flames of propane flowing into 17% oxygen. A heating wire was used.

Results for extinction time and extinction diameter as a function of flowrate for propane issuing into 17% oxygen are shown in Figure 4.6. This figure is similar to Figure 4.5 except the fuel is now propane and the fuel is issued from the burner instead of being in the ambient. Similar to the results for ethylene, there is good agreement between the experiment and computation for the extinction diameters and they seem to have the same square root flowrate dependence. Although the extinction diameters agree between the model and experiment, the numerical results for extinction time at low flowrates show a trend that does not agree with experiments or the results from Figure 4.5 at first glance. Further inspection of the experimental results for both ethylene and propane reveals that there is a peak in the extinction time in between the high and low flowrate limits. For the ethylene case, the peak appears for a flowrate of about 5 mg/s. For the propane case, there is a gap in the experimental data but there are signs of a peak where the flowrate is slightly greater than 1 mg/s. These peaks observed in the experimental data led to the hypothesis that in Figure 4.6 the increase in the extinction time with decreasing flowrate is the end of a peak. There has to be a point where the flowrate is low enough that the heat loss to the burner

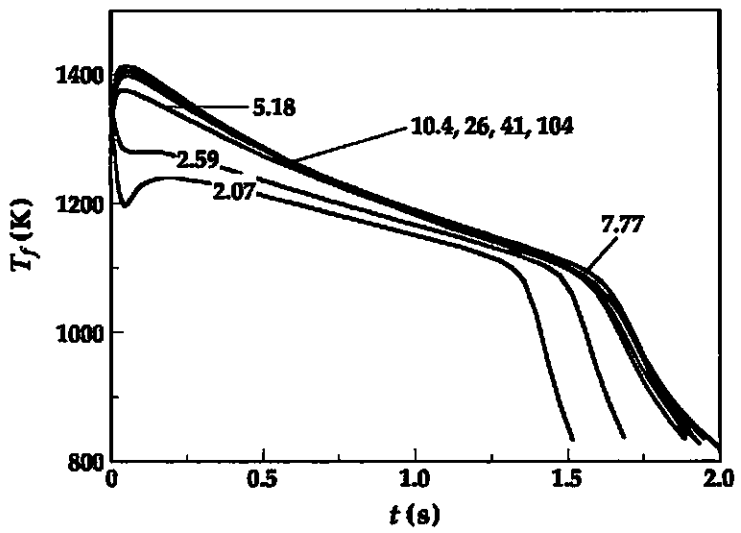

Figure 4.7: Modeled flame temperatures for flames of oxygen flowing into 4% ethylene at different flowrates. The numbers on the graph represent oxygen flowrates in mg/s.

causes a reduction in the extinction time. Unfortunately the instability of the numerical code at low flowrates has prevented the production of results for flowrates lower than 0.7 mg/s. Further study will be necessary to explain the numerical results of Figure 4.6 at low flowrates. For now we will focus on the asymptotic behavior of the extinction time at high flowrates for both cases.

To understand the progression of the flames to extinction, the transient behavior of the flame temperatures was observed. Figure 4.7 illustrates the numerical results for flame temperature as a function of time for the case with oxygen flowing into diluted ethylene. At high flowrates, the results are similar to Figure 4.4, where the temperatures first increase slightly and then continuously decrease until extinction around 1.7 s. The rapid drop in flame temperature, indicating the end of heat generation reveals the extinction. For flames with a flowrate of 2.6 mg/s or less, a different trend is observed. Here the temperature initially decreases and then increases before begining its slow decrease to extinction due to radiative heat loss. For flowrates greater than 5.1 mg/s, the temperature versus time curves are practically identical. Thin-filament pyrometry measurements, shown in Figure

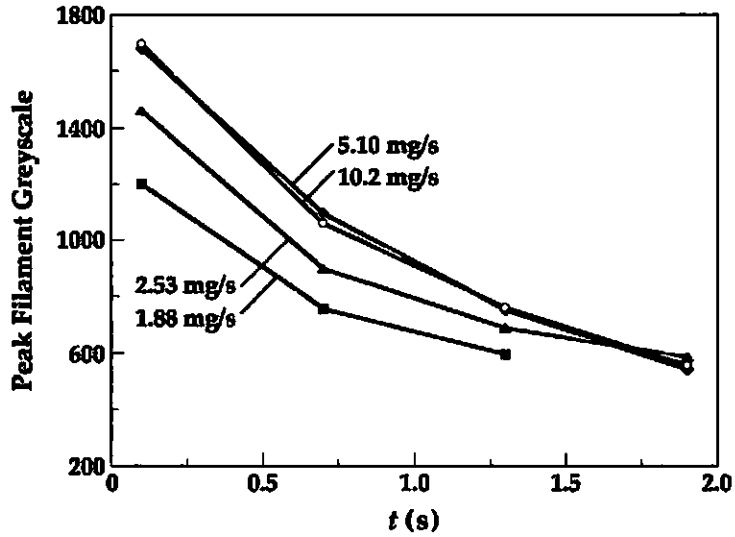

Figure 4.8: Thin-filament pyrometry average peak greyscales for flames of oxygen flowing into 5% ethylene. These are non-extinguishing flames except at 1.88 and 2.53 mg/s.

4.8, are consistent with the numerical results in that for flowrates of 5.1 mg/s and above, the temperatures are nearly identical while for lower flowrates the temperature decreases with decreasing flowrate. The results were taken at a slightly higher ethylene concentration (5% as opposed to 4%) to ensure the flames did not extinguish prematurely due to the presence of the filaments.

Due to the flame size increasing with flowrate it might be expected that the larger flames would extinguish earlier because of the greater radiative losses. Although steady-state theories of extinction (Chao et al. 1990, Atreya & Agrawal 1998, Mills & Matalon 1998) indicate that increasing flame size leads to extinction due to the greater radiative loss with flame size this cannot be applied to predict the time to extinction for transient flames.

To further understand the reason the extinction time becomes independent of flowrate, the radiative heat loss rate, chemical heat release rate, and ratio are plotted versus oxygen flowrate for oxygen flowing into diluted ethylene in Figure 4.9. These values correspond to the different ethylene cases in Figure 4.5. The values are taken just before extinction. Clearly as flowrate and flame diameter increase, radiative loss increases, but at the same

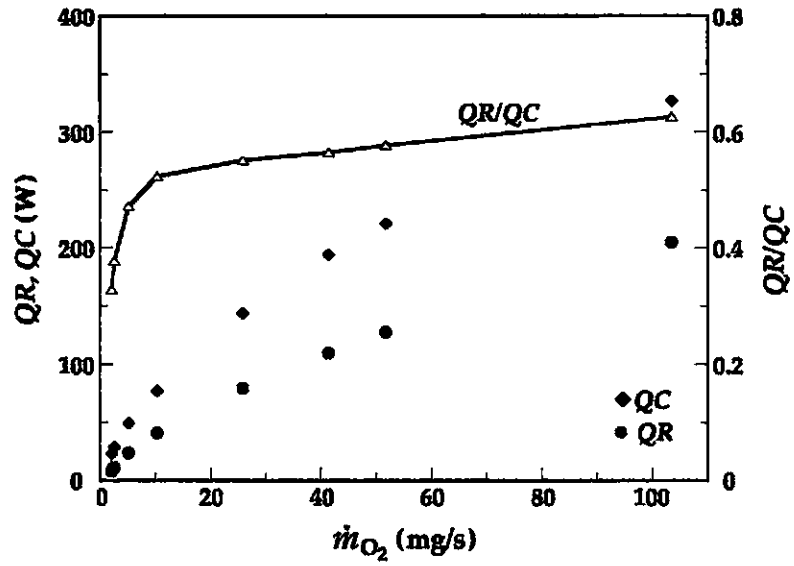

Figure 4.9: Modeled radiation loss and heat release near extinction for different flowrates plotted vs. flowrate. Results shown are for flames of oxygen flowing into 4% C_2H_4. The radiative loss is represented by QR and the heat release rate is QC.

time the heat release rate increases due to the flame surface area increasing. Figure 4.9 indicates that the ratio QR/QC, which is the primary variable affecting extinction, initially increases rapidly but begins to level off above flowrates of about 5 mg/s. The small change in QR/QC with flowrate would explain the reason that the flames at higher flowrates have similar temperature versus time relationships even though the flame sizes and mass flowrates are different.

Originally, it was thought that radiative heat loss scaled with volume and not surface area, however, the nearly constant ratio of QR/QC suggests otherwise. The radiative heat loss should scale with flame surface area to be proportional to the heat release rate. To understand the radiative heat loss a plot of the mole fraction of CO_2 for the flames of Figure 4.7 were constructed in Figure 4.10. Both CO_2 and water strongly influence radiative heat loss but CO_2 will be the focus with the recognition that the key findings will be similar for water vapor. Referring to Figure 4.10, while the thickness of the CO_2 layer increases with flowrate on the inside of the flame, it is evident that the thickness outside the flame is

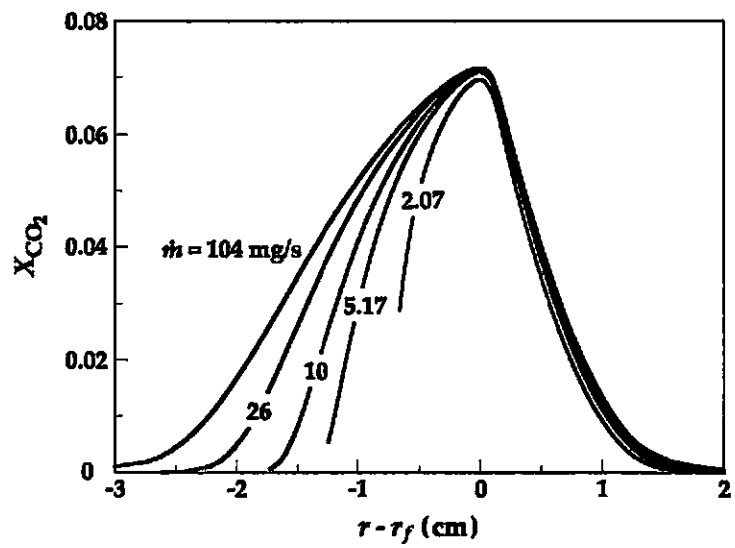

Figure 4.10: Modeled concentration of CO_2 as a function of radius. The flames involve oxygen flowing into 4% ethylene in nitrogen at various flowrates. Oxygen flowrates (in mg/s) are labeled for each curve. The curves correspond to times of 0.5s after ignition. Symbols r and r_f indicate radius and radius at peak temperature, respectively.

nearly constant and it is this region that dominates the radiative loss from the flame. There are several reasons why the outside layer dominates the radiative loss. First, the volume of each layer scales with the square of the radius and since the outside of the flame has a larger radius its volume will be considerably larger. Second, since the radiation is modeled as optically thick, some of the radiation from the inside layer will be reabsorbed by the outside layer and thus will not constitute a loss.

The consistency in the outer layer thickness implies that the volume of the radiative zone increases with surface area. When the heat loss to the burner is negligible, the ratio of radiative heat loss to heat release rate should level off since both QR and QC scale with flame surface area. With this explanation it is also clear why radiative loss grows with time. In the outer layer the spread rate of the radiating species is due to diffusion, not mass flowrate, and since there is an infinite domain there is no characteristic length associated with the spread. From simple scaling laws, the growth of the diffusion thickness is given by $\delta \sim (Dt)^{1/2}$ where D is the diffusivity and t is the time. Choosing an approximate value 1

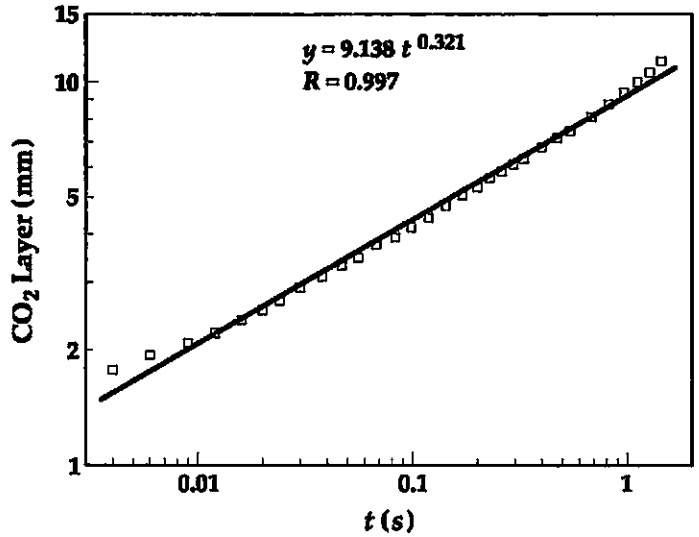

Figure 4.11: Modeled thickness of 65% of the CO_2 layer as a function of time. The data is plotted on a log-log scale. The data shown is for a flame of oxygen issuing into 4% ethylene at 41 mg/s.

cm^2/s for D and 0.5 s for t, yields a diffusion thickness of 0.7 cm, which is consistent with the thickness of the outer layer in Figure 4.10. Figure 4.11 shows how the actual thickness of the CO_2 layer varies with time, based on the numerical results. The fact that the power law fit shows an exponent of 0.32 instead of 0.5 is likely the result of the $D \sim T^{1/2}$ dependence.

To see whether the dependence of the CO_2 are unique to ethylene, a plot was constructed to compare the CO_2 profiles from propane with ethylene. From Figure 4.12 it is apparent that the CO_2 mole fraction profiles are similar in an inverse ethylene and normal propane flame. The predictions from Figure 4.10 and 4.12 indicate that the CO_2 profiles are independent of fuel type and convection direction (normal and inverse). The independence of the CO_2 profiles, with respect to fuel type and convection direction explain why the flames have similar extinction time. Since the growth of the diffusion layer is the primary determinant of extinction, the fuel type and flame configuration are secondary.

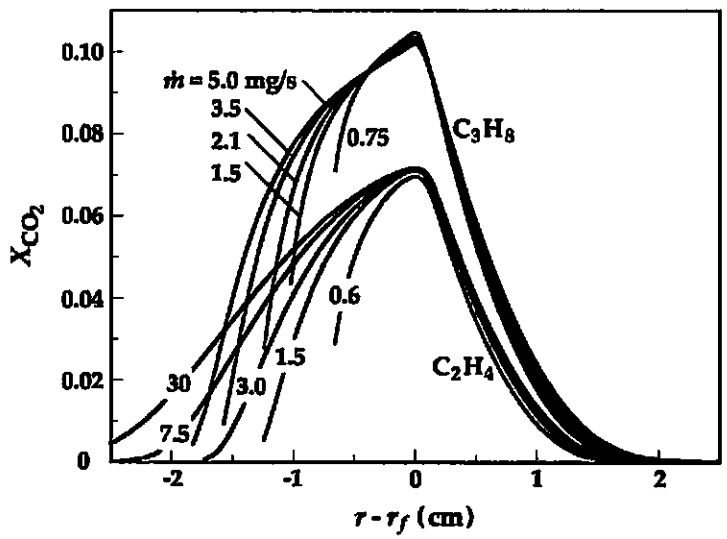

Figure 4.12: Comparison of modeled CO_2 mole fractions for flames of C_2H_4 flowing into 11% O_2 and C_3H_8 flowing into 17% O_2. Flowrates (in mg/s) are labeled for each curve. The curves correspond to times of 0.5s after ignition.

Chapter 5

CONCLUSIONS

5.1 Numerical and Experimental Observations

With regard to the first section of the results, this work sought to validate or explain the shortcomings of the numerical model and further using the numerical results along with experiments to investigate the Lewis number effect. The accuracy of the model was accessed through comparison between the numerical and experimental results of transient flame diameters and flame temperature (t = 2s) for four ethylene flame configurations. The difference in flame temperature (steady-state without radiation) for the four ethylene flames (with the same T_{ad}) was also investigated by considering the Lewis number effect and intermediate species loss.

The significant findings of this study are:

1. The numerical model has the ability to qualitatively predict the growth of the flame diameters over time but lacks accuracy when compared to the experiments. Good quantitative agreement can only be obtained by increasing the transport properties by 30% or decreasing the flow rates by 25% in the model.

2. Spherical diffusion flames with various convection directions and stoichiometric mixture fractions (with identical T_{ad}) reveal a decrease in flame temperature with an increase in flame size. The transient model indicated that the reduction in temperature was due to gas-phase radiative losses.

3. Inverse spherical diffusion flames with diluted fuel in the ambient experience a loss of intermediate species to the ambient which results in a small reduction in flame temperatures.

4. The Lewis number of the ambient reactant can have a profound effect on flame temperature. For example, computations which employed a simplified one-step reaction in the reaction sheet limit showed, for Le near unity, a 10% increase in Le is predicted to decrease flame temperature by 200 K. The numerical model with detailed chemistry and transport revealed that flame (d) had a flame temperature about 200K cooler than the other three flames and in fact had an ambient Le around 25% higher than these flames. These results could have important implications for extinguishing fires in spacecraft since CO_2 is used to extinguish fires and dilution with CO_2 results in a decrease in Le.

5.2 Radiative Extinction

The major findings from studying radiative and kinetic extinction during transient burning are:

1. For the flames that extinguished within the 2.2 s of available test time, two modes of extinction were identified: hole and base extinction. The onset times of both modes were the same within experimental uncertainties.

2. The experiments and computations indicate that the flames generally grow and cool from ignition to extinction. Except at low flowrates, flame temperatures usually decrease with time and the rate of decrease is independent of flowrate.

3. For a given flame configuration, the flame diameters at extinction scale with the square root of the flowrate.

4. At low flowrates, extinction time increases with flowrate owing to a reduction in burner heat loss. At high flowrates, radiative extinction is observed and the time to reach extinction becomes independent of flowrate.

5. Radiative heat loss is dominated by the region outside of the flame which scales with the flame surface area. For transient flames, heat release rate also scales with surface area resulting in the radiative loss fraction being relatively independent of flowrate.

References

Antal, M. J. (2004), 'Peak in world oil production', Lecture in *Chemical Reactor Design.*

Atreya, A. & Agrawal, S. (1998), 'Effect of radiative heat loss on diffusion flames in quiescent microgravity atmosphere', *Combustion and Flame* **115**, 372—382.

Bradley, D. & Entwistle, A. G. (1961), 'Determination of the emissivity, for total radiation, of small diameter platinum-10% rhodium wires in the temperature range 600-1450°C', *British Journal of Applied Physics* **12**, 708—711.

Burke, S. P. & Schumann, T. E. W. (1928), 'Diffusion flames', *Industrial and Engineering Chemistry* **20**, 998—1004.

Carlson, B. G. & Lathrop, K. G. (1968), *Computing Methods in Reactor Physics*, Gordon and Breach, New York, NY.

Carlson, R. (2005), 'Brave new oil-scarce world', *Honolulu Weekly* **15**(18).

Chao, B. H., Law, C. K. & T'ien, J. S. (1990), 'Structure and extinction of diffusion flames with flame radiation', *Proc. Combust. Inst.* **23**, 523—531.

Chung, S. H. & Law, C. K. (1983), 'Structure and extinction of convective diffusion flames with general Lewis numbers', *Combustion and Flame* **52**, 59—79.

Dietrich, D. L., Haggard, J. B., Dryer, F. L., Nayagam, V., Shaw, B. D. & Williams, F. A. (1996), 'Droplet combustion experiments in spacelab', *Proc. Combust. Inst.* **26**, 1201—1207.

Grcar, J. F. (1992), The twopnt program for boundary value problems, Technical Report SAND91-8230, Sandia National Laboratories.

Hirschfelder, J. O., Curtiss, C. F. & Bird, R. B. (1964), *The Molecular Theory of Gases and Liquids*, Wiley and Sons, Hoboken, NJ.

Ignatius, D. (2004), 'As oil prices boil . . .', *The Washington Post* p. A19.

Kee, R. J., Dixon-Lewis, G., Warnatz, J., Coltrin, M. E. & Miller, J. A. (1988), A fortran computer code package for the evaluation of gas phase multicomponent transport properties, Technical Report SAND86-8246, Sandia National Laboratories.

Kee, R. J., Grcar, J. F., Smooke, M. D., Miller, J. A. & Meeks, E. (1987), A program for modeling steady, laminar, one-dimensional premixed flames, Technical Report SAND85-8240, Sandia National Laboratories.

Kee, R. J., Rupley, F. M. & Miller, J. A. (1989), Chemkin-II: A fortran chemical kinetics package for the analysis of gas phase chemical kinetics, Technical Report SAND89-8009B, Sandia National Laboratories.

Law, C. K. (1975), 'Asymptotic theory for ignition and extinction in droplet burning', *Combustion and Flame* **24**, 89—98.

Law, C. K. & Chung, S. H. (1982), 'Steady state diffusion flame structure with Lewis number variations', *Combustion Science and Technology* **29**, 129—145.

Liñán, A. (1974), 'The asymptotic structure of counterflow diffusion flames for large activation energies', *Acta Astronautica* **1**, 1007—1039.

Liu, F., Guo, H., Smallwood, G. J. & Gulder, O. L. (2001), 'The chemical effects of carbon dioxide as an additive in an ethylene diffusion flame: Implications for soot and nox formation', *Combustion and Flame* **125**, 778—787.

Liu, F., Smallwood, G. J. & Gülder, O. L. (2000), 'Asymptotic analysis of radiative extinction in counterflow diffusion flames of nonunity lewis numbers', *Combustion and Flame* **121**, 275—287.

Maun, J. D., Sunderland, P. B. & Urban, D. L. (2006), Thin-filament pyrometry with a digital still camera. Paper presented at the Spring meeting of the Central States Section of the Combustion Institute, Cleveland, Ohio, May 21-23.

McBride, B. J. & Gordon, S. (1996), A computer program for calculation of complex chemical equilibrium compositions and applications, Technical Report RP-1311-P2, NASA Lewis Research Center.

Middha, P., Yang, B. & Wang, H. (2002), 'A first-principle calculation of the binary diffusion coefficients pertinent to kinetic modeling of hydrogen/oxygen/helium flames', *Proc. Combust. Inst.* **29**, 1361—1369.

Mills, K. & Matalon, M. (1997), 'Burner-generated spherical diffusion flames', *Combustion Science and Technology* **129**, 295—319.

Mills, K. & Matalon, M. (1998), 'Extinction of spherical diffusion flames in the presence of radiant loss', *Proc. Combust. Inst.* **27**, 2535—2541.

Nayagam, V., Haggard, J. B., Colantonio, R. O., Marchese, A. J., Dryer, F. L., Zhang, B. L. & Williams, F. A. (1998), 'Microgravity n-heptane droplet combustion in oxygen-helium mixtures at atmospheric pressure', *AIAA* **36**(8), 1369—1378.

Paul, P. & Warnatz, J. (1998), 'A re-evaluation of the means used to calculate transport properties of reacting flows', *Proc. Combust. Inst.* **27**, 495—504.

Pitts, W. M. (1996), 'Thin-filament pyrometry in flickering laminar diffusion flames', *Proc. Combust. Inst.* **26**, 1171—1179.

Rothman, L. S., Rinsland, C. P., Goldman, A., Massie, S. T., Edwards, D. P., Flaud, J.-M., Perrin, A., Camy-Peyret, C., Dana, V., Mandin, J.-Y., Schroeder, J., Mccann, A., Gamache, R. R., Wattson, R. B., Yoshino, K., Chance, K. V., Jucks, K. W., Brown, L. R., Nemtchinov, V. & Varanasi, P. (2003), 'The HITRAN molecular spectroscopic database: edition of 2000 including updates through 2001', *Journal of Quantitative Spectroscopy and Radiative Transfer* **82**, 5—44.

Santa, K., Sun, Z., Chao, B. H., Sunderland, P. B., Axelbaum, R. L., Urban, D. L. & Stocker, D. P. (n.d.), Numerical and experimental observations of spherical diffusion flames. Unpublished work.

Smith, G. P., Golden, D. M., Frenklash, M., Moriarty, N. W., Eiteneer, B., Goldenberg, M., Bowman, C. T., Hanson, R. K., Song, S., Jr., W. C. G., Lissianski, V. V. & Qin, Z. (n.d.), 'Gri-mech 3.0', http://www.me.berkeley.edu/gri_mech/.

Sunderland, P. B., Axelbaum, R. L., Urban, D. L., Chao, B. H. & Liu, S. (2003), 'Effects of structure and hydrodynamics on the sooting behavior of spherical microgravity diffusion flames', *Combustion and Flame* **132**, 25—33.

Sunderland, P. B., Urban, D. L., Stocker, D. P., Chao, B. H. & Axelbaum, R. L. (2004), 'Sooting limits of microgravity spherical diffusion flames in oxygen-enriched air and diluted fuel', *Combustion Science and Technology* **176**(12).

Tse, S. D., Zhu, D., Sung, C.-J., Ju, Y. & Law, C. K. (2001), 'Microgravity burner-generated spherical diffusion flames: experiment and computation', *Combustion and Flame* **125**, 1265—1278.

Vilimpoc, V. & Goss, L. P. (1988), 'Sic-based thin-filament pyrometry: theory and thermal properties', *Proc. Combust. Inst.* **22**, 1907—1914.

Wu, X., Law, C. K. & Fernandez-Pello, A. C. (1982), 'A unified criterion for the convective extinction of fuel particles', *Combustion and Flame* **44**, 113—124.

Zapka, M. (2006), 'Peak oil and the end of cheap-and-easy-oil', UHM Physics Department Seminar.